The near-bed flow structure and bed shear stresses within emergent vegetation canopies

M. Conde-Frias[1,2,3], M. Ghisalberti[1,2], R. Lowe[1,2,3], M. Abdolahpour[1,2,3], and V. Etminan[1]

[1] Oceans Graduate School, University of Western Australia, Perth, Australia.

[2] UWA Oceans Institute, University of Western Australia, Perth, Australia.

[3] ARC Centre of Excellence for Coral Reef Studies, University of Western Australia, Perth, Australia.

Corresponding author: Mario Conde-Frias (mario.conde-frias@research.uwa.edu.au)

Key Points

- Vegetated flows are characterized by strong spatial variability of key near-bed flow characteristics on the scale of the vegetation elements.
- The thickness of the bottom boundary layer (locally and in the mean) is strongly controlled by the near-bed turbulent kinetic energy (TKE).
- Spatial changes of near-bed TKE induce changes in the BBL thickness, which in turn generates strong spatial variability of bed shear stress

(The above elements should be on a title page)

Abstract

The structure of the bottom boundary layer (BBL) in aquatic flows influences a range of biophysical processes, including sediment transport, hyporheic exchange, and biofilm formation. While the structure of BBL above bare sediment beds has been well studied, little is known about the complex near-bed flow structure within canopies of aquatic vegetation. In this study, we used high-resolution laboratory measurements and numerical Large Eddy Simulations to investigate the near-bed mean and turbulent flow properties within staggered-ordered emergent canopies under a wide range of flow and canopy conditions. There is strong horizontal variability of key near-bed flow characteristics on the scale of the vegetation elements. Measurement locations that provide single-point flow characteristics closest to the spatially-averaged values were identified. The spatially-averaged BBL thickness is influenced strongly by canopy density. This impact of canopy density is engendered through its direct control of near-bed turbulent kinetic energy (TKE), which in turn is negatively correlated with BBL thickness, both locally in a given flow and across the range of flow conditions studied here. A model based on the near-bed TKE is developed to predict the BBL thickness and, ultimately, the bed shear stress. The strong agreement between model predictions and experimental data may explain why both TKE and bed shear stress may be seen as drivers of sediment transport processes in vegetated flows. These findings provide new insights into the physical links between near-bed flow variables and therefore contribute to the understanding of some of the complex biophysical processes present in vegetated flows.

1 Introduction

Canopies formed by aquatic vegetation provide numerous ecosystem services in riverine and coastal environments. For instance, these canopies can help to stabilize mobile sediment beds by transforming an erosional bed into a depositional one (Shields et al., 1995). The enhanced drag forces induced by the canopy can also modify circulation and sediment transport pathways, which over time can shape the morphological evolution of riverine and coastal systems (Ward et al., 2000; Hooke, 2007; van Katwijk et al., 2010; Vargas-Luna et al., 2015). Moreover, canopies can mitigate the impact of coastal hazards (i.e. coastal erosion, flooding, etc.) by dissipating wave energy (Massel et al., 1999; Türker et al., 2006; Lowe et al., 2007). Finally, aquatic canopies help shape a wide range of environmental and ecological processes, such as improving water quality

(Cundy et al., 2005) and promoting biodiversity by creating sheltered habitats (Hemminga & Duarte, 2000).

The interaction between hydrodynamics and sediment processes in aquatic systems is controlled by the layer of water adjacent to the bed, the bottom boundary layer (BBL) (Nowell & Jumars, 1984; Wüest & Lorke, 2003; Trowbridge & Lentz, 2018). The physical structure of this layer governs several critical physical, chemical, and biological processes, such as sediment transport (Yalin, 1977; van Rijn, 2007a, 2007b), hyporheic exchange (Grant et al., 2018; Roche et al., 2018; Voermans et al., 2018) and biofilm formation (Beer & Kühl, 2001). Due to its importance, the structure of the BBL above bare beds has been widely investigated, with the vertical structure of mean velocities, turbulence levels, and shear stresses well-known. However, the influence of vegetation on BBL characteristics is poorly understood due to the fine-scale variability of the flow within aquatic vegetation and the difficulties associated with obtaining high-resolution measurements within this layer. Thus, studies that directly resolve near-bed velocities, stresses, and turbulence intensities in vegetated flows are of paramount importance in understanding the variation of near-bed hydrodynamic parameters (including those relevant to sediment transport) with canopy characteristics.

This study aims to characterize the near-bed mean and turbulent flow structure within the BBL in emergent canopies. By combining laboratory measurements and numerical simulations for a wide range of canopy densities and flow conditions, we determine BBL thickness ($\mathcal{O}$(mm)) and its variation with flow and canopy characteristics. In addition, we examine the vertical and horizontal structure of the mean velocity, near-bed stresses, and turbulent kinetic energy within the BBL. Finally, we elucidate the link between bed shear stress and turbulent kinetic energy, which explains why both have been used as predictors of sediment transport in vegetated systems.

1.1 Flow and vegetation interaction

Given the vast diversity of plant morphology in natural environments, canopies are often modelled simply as arrays of rigid dowels (Nepf & Ghisalberti, 2008; Abdolahpour et al., 2018) arranged in different configurations (e.g. squared, staggered or randomly). The key geometric characteristics of such a model canopy are the diameter (d) and the height (h) of the vegetation elements, as well as the number of elements per bed area (n). A nondimensional measure of the

canopy density is the solid volume fraction occupied by the canopy elements ϕ, equal to $(\pi/4)ad$ for cylindrical dowels, with a $(= nd)$ being the frontal area per canopy volume. The variation of these canopy properties can greatly affect the mean and turbulent velocity structure within canopies by controlling the drag exerted on the flow (Nepf & Vivoni, 2000; Nepf, 2012a).

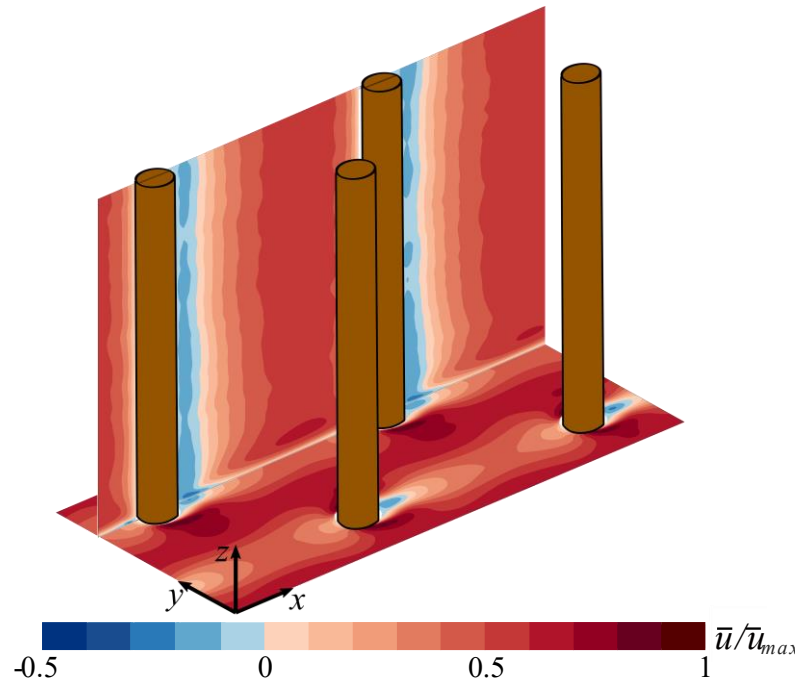

Figure 1. Typical structure of the mean streamwise velocity ($\bar{u}$) field in an emergent canopy normalized by the local maximum velocity ($\bar{u}_{max}$), obtained here from numerical Large Eddy Simulation. Element wakes, and the tortuous nature of the flow within the canopy create high spatial variability at the element scale.

Due to the obstructions presented by canopy elements and element wakes, the flow is forced to move around each element, such that the velocity field is spatially heterogeneous at the scale of the element diameter (Figure 1). To account for this element-scale spatial heterogeneity, the double-averaging procedure was employed, whereby instantaneous velocity statistics (ζ) are first decomposed into a temporal average (indicated by an overbar) and deviations from it (indicated by a prime), such that $\zeta = \bar{\zeta} + \zeta'$. Time-averaged quantities are further decomposed into a spatial mean and deviation, with angular brackets denoting a horizontal average at height z over several canopy elements and double primes indicating deviations from the horizontal mean ($\bar{\zeta} = \langle\bar{\zeta}\rangle + \bar{\zeta}''$) (Raupach & Shaw, 1982; Nikora et al., 2001). The double-averaged Navier-Stokes

equation in the streamwise direction for steady and uniform flow through aquatic vegetation becomes:

$$0 = gsin\theta - \frac{1}{\rho}\frac{\partial\langle\bar{p}\rangle}{\partial x} - \frac{\partial}{\partial z}\left[\langle\overline{u'w'}\rangle - \langle\bar{u}''\bar{w}''\rangle + \nu\frac{\partial\langle\bar{u}\rangle}{\partial z}\right] - \frac{1}{2}\frac{C_D a}{(1-\phi)}\langle\bar{u}\rangle^2, \quad (1)$$

$$(i) \quad (ii) \quad (iii) \quad (iv) \quad (v) \quad (vi)$$

(Raupach and Shaw 1982) where u and w are the velocity components in the directions of x (streamwise direction) and z (vertical direction), respectively, ρ is the water density, ν is the kinematic viscosity, θ is the bed slope, C_D is the canopy drag coefficient, g is gravitational acceleration, and *p* is pressure. Term (*i*) is the gravity force, term (*ii*) is the pressure gradient, term (*iii*) represents the spatially-averaged Reynolds stress, term (*iv*) the momentum flux associated with spatial correlations of time-averaged velocity fields (termed the 'dispersive' stress) and term (*v*) the spatially-averaged viscous stress. The sum of these three terms defines the total fluid shear stress, τ. Term (*vi*) represents the spatially averaged drag associated with the canopy elements (Nepf, 2012a).

The relative importance of each term in Eq. (1) depends on the properties of the flow, vegetation, and height above the bed. In emergent canopies, the momentum equation can generally be simplified into a balance between pressure gradient and the canopy drag over most of the water column (Nepf, 2012a). However, within the strong shear of the BBL, other terms in Eq. (1) may become significant. As little is known of the complex near-bed flow structure within canopies, we aim here, using a combination of experimental and numerical approaches, to directly resolve the mean velocity structure and stress components (terms $(iii), (iv)$ and (v) in Eq. 1) in the region adjacent to the bed across a wide range of canopy densities.

1.2 Interaction between hydrodynamics and sediment transport

Sediment transport in unvegetated channels is typically estimated from empirical formulations based on the shear stress at the bed, τ_b (often expressed in terms of friction velocity, $u_* = \sqrt{\tau_b/\rho}$) (van Rijn, 1987; James et al., 2002; Jordanova & James, 2003). In sediment transport models developed for bare beds, the role of turbulence in suspending and transporting sediment

may be considered implicitly, given the inherent proportionality between the mean bed stress and turbulence intensities in the bare bed boundary layer (Stapleton & Huntley, 1995; Nepf, 1999). However, this proportionality breaks down in canopy flows, where the turbulence can be predominantly generated in plant wakes rather than at the bed (Nepf, 1999, 2012b). As a consequence, predictive models developed for bare beds are unlikely to be quantitatively applicable to vegetated environments.

Despite the fundamental differences between unvegetated and vegetated flows, some studies (Jordanova & James, 2003; Kothyari et al., 2009; Larsen et al., 2009) have suggested that bed shear stress may control sediment transport within vegetation. However, it is still not well established how canopies modify bed shear stresses. To bridge this gap, several methods for estimating bed shear stress within canopies have been proposed (e.g. Jordanova & James, 2003; Kothyari et al., 2009; Yang et al., 2015; Etminan et al., 2018). In general, these methods are based on one of the following approaches: 1) estimation of the bed shear stress by the subtraction of the element drag (term (*vi*) in Eq. 1) from the driving forces (terms (*i*) and (*ii*) in Eq. 1) and 2) estimation of bed shear from velocity measurements in the near-bed region. The main limitation of the first approach is that both variables (drag and the driving force) are often orders of magnitude larger than the bed shear stress, resulting in potentially large errors when computing small differences. Similarly, methods based on the second approach require measurements of the velocity gradient within the viscous-stress dominated sublayer (H_{v}) in vegetated flows (region immediately adjacent to the bed where turbulence is negligible, and the viscous stress dominates the total stress). These methods are experimentally tricky, given that the thickness of this layer is typically $\lesssim \mathcal{O}$(mm). Despite these difficulties, Yang et al. (2015) developed a model to estimate the bed shear stress in aquatic vegetation based on the linear variation of the stress within the viscous-stress dominated sublayer (H_{v}). In this model, the temporally- and spatially-averaged bed shear stress ($\langle\bar{\tau}_b\rangle$) is estimated from the streamwise velocity above the BBL $\langle\bar{u}\rangle$ and H_{v} (taken in their study as $\min(\frac{d}{2}, (22 \pm 3)\nu/u_*)$). Although this model represents a step forward in the prediction of bed shear stress in emergent aquatic vegetation, it is still limited since it does not embed the significant impact that seems to have the canopy density in H_{v} and ultimately in the bed shear stress. To address some of the limitations found in the previous model, an alternative estimate of the thickness of H_{v} can be inferred by assuming a balance between the production of the

151 turbulent kinetic energy in the cylinder wakes and the viscous dissipation of TKE near the bed
152 (Etminan et al. 2018).

153 Several studies of sediment dynamics in vegetated systems (Tinoco & Coco, 2014, 2016,
154 2018; Yang et al., 2016; Yang & Nepf, 2018, 2019) have concluded that sediment transport
155 processes are correlated with levels of near-bed turbulence (a combination of the turbulence
156 produced in element wakes and the BBL). For instance, the threshold for sediment motion in
157 emergent vegetation was driven by a critical value of the turbulent kinetic energy, which can be
158 deduced from the critical velocity required for sediment motion in bare beds (Yang et al., 2016).
159 In a subsequent study, a reinterpretation of the bed-shear-stress-based Einstein-Brown bed-load
160 transport model in terms of the turbulent kinetic energy was proposed to improve predictions of
161 bed-load transport within aquatic vegetation (Yang & Nepf 2018). Finally, improvements in the
162 prediction of suspended sediment concentrations within aquatic vegetation were found when the
163 effect of wake-generated turbulence was incorporated into traditional sediment transport models
164 developed for bare beds (based on the Shields parameter) (Tinoco & Coco, 2016). Despite the
165 evidence of the strong role of the TKE on sediment transport within vegetated regions, from a
166 mechanistic perspective, turbulent kinetic energy does not represent a force on sediment grain,
167 whereas bed shear stresses do (as by definition represent the force exerted on the bed).

168 Previous studies have suggested that sediment transport models based on the bed shear
169 stress fail within vegetated regions because they do not account for the vegetation-generated
170 turbulence. In other words, they suggest that the 'external' turbulence from the plants and the bed
171 shear stress are decoupled in these flows (Tinoco & Coco, 2018; Yang & Nepf, 2018). However,
172 we believe that the complete unlink between the TKE and bed shear stress within vegetated flows
173 is not necessarily valid.

174 Here, we examine the links between bed shear stresses and near-bed TKE levels in
175 emergent canopies and hypothesize that the TKE generated by the vegetation increases vertical
176 momentum transport, which in turn creates a thinner boundary layer and ultimately an increase in
177 the bed shear stress. Accordingly, one of the priorities of this integrated experimental and
178 numerical study is to look at the extent to which the near-bed turbulent kinetic energy controls the
179 BBL thickness and, ultimately, the bed shear stresses within aquatic vegetation.

2 Methodology

2.1 Experimental configuration

Experiments were carried out in a 20-m-long, 0.6-m-wide, and 0.45-m-deep recirculating flume in the Coastal and Offshore Engineering Laboratory at the University of Western Australia (Figure 2a).

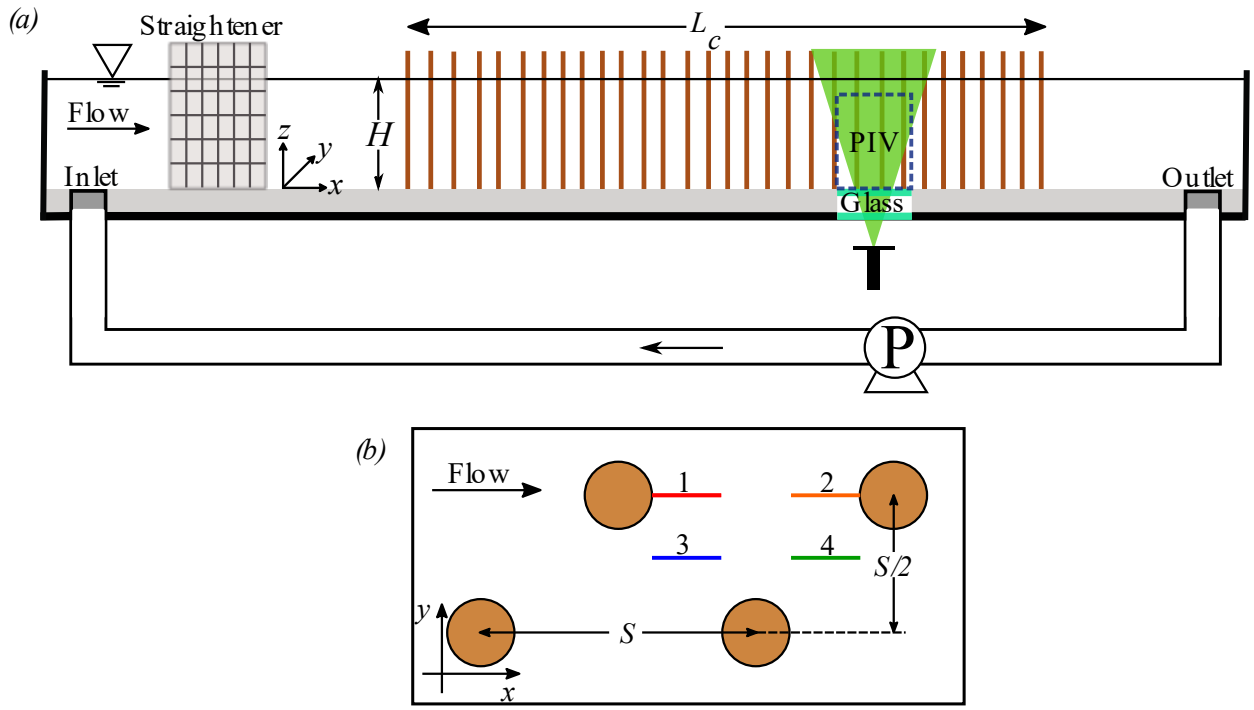

Figure 2. (a) Side view of the experimental setup. The flow depth was fixed at $H = 26.5$ cm. (b) Top view of the staggered canopy array, with PIV measurements taken at the four transects indicated by the coloured lines. S is the distance between the elements.

The flow, from 6.4- 27.5 L/s, was generated by a recirculating pump. A honeycomb flow straightener was installed on the upstream side of the flume to promote uniform parallel flow. Experiments were designed to elucidate the impact of canopy density and flow speed on the near-bed flow structure in emergent aquatic vegetation. Given that most emergent aquatic vegetation is characterized by rounded shoots of high stiffness (Nepf, 2012a), simplified rigid elements (cylindrical wooden dowels with a diameter $d = 0.65$ cm and height of 30 cm) were used as an idealized proxy for emergent canopies. The dowels were fixed to a perforated PVC baseboard in a staggered pattern (Figure 2b) across the channel width. To ensure fully-developed canopy flow,

198 the total length of the canopy model (L_c) was at least five times the drag length scale L_d, defined
199 as $L_d = (C_D a)^{-1}$ (Lowe et al., 2005; Morse et al., 2002). To fully cover typical field ranges, four
200 canopy densities (ϕ) ranging from 0.016 to 0.098 were studied. For each canopy density, five flow
201 conditions (U_b) were tested. Here U_b is the bulk channel velocity, defined as $Q/(WH)$, with W the
202 flume width and H the water depth (which was kept constant at 26.5 cm for all cases). This
203 experimental program is summarized in Table 1.

204 **Table 1. Experimental conditions**

Density, ϕ	Frontal area, a [m^{-1}]	Bulk channel velocity, U_b [m/s]
0.016	3.1	0.04, 0.06, 0.09, 0.13, 0.18
0.025	5.2	
0.044	9.3	
0.098	20.8	

205 **2.2 Particle Image Velocimetry**

206 Velocity measurements were obtained using particle image velocimetry (PIV) at four
207 locations within the array (Figure 2b). The PIV system consisted of a 300 mW continuous-wave
208 (CW) 532 nm DPSS laser with a 60° fan angle and a light sheet thickness of 1 mm. Images were
209 recorded for 7 min with a 12-bit, 1024 x 1024, CMOS camera (Photron FASTCAM SA3),
210 equipped with a Nikon AF Nikkor 50mm f/1.4d lens. The frame rate of the camera was adjusted
211 to ensure that maximum particle displacement was always less than a quarter of the interrogation
212 window (Raffel et al., 2012) and ranged from 125-500 fps. Polyamide particles with a nominal
213 diameter of 43 – 55 μm and a specific gravity of 1.04 were used as tracer particles.

214 The analysis of recorded images was carried out using the open software PIVlab (Thielicke
215 & Stamhuis, 2014). Before the PIV analysis, all images were pre-processed to enhance the
216 contrast. Velocity fields were determined indirectly by finding the displacement of particles
217 between two consecutive frames through a multi-pass window deformation scheme with
218 decreasing interrogation window sizes. Depending on the experiment, two or three successive 50%
219 size passes with 50% overlapped interrogation windows (64 × 64 to 16 × 16 pixels or 32 × 32 to
220 16 × 16 pixels) along with a Gaussian sub-pixel interpolation scheme (Nobach & Honkanen, 2005;
221 Raffel et al., 2012) were used to obtain high-resolution velocity maps near the bed. However, due

to the finite number of particles, fewer particles in each window are cross-correlated as the interrogation area gets smaller, creating more spurious velocity vectors (Raffel et al., 2012). To overcome this, an ensemble correlation approach was implemented (Santiago et al., 1998; Meinhart et al., 2000;), whereby cross-correlation for several image pairs is computed, with correlation maps then averaged for peak detection and calculation of velocity components. This approach increases the SNR (as more image pairs are ensemble-correlated), allowing to obtain high-resolution velocity fields even with low particle densities. In each experiment, the number of images for the ensemble correlation was chosen to provide velocity data at a minimum frequency of 25 Hz, which, for the frame rate used, were between 5-20 image pairs. Erroneous velocity vectors (outliers) were identified and eliminated through a combination of a global standard deviation filter and a local median filter, which evaluates the velocity fluctuation with respect to the median in 3 x 3 neighbourhoods around a central vector (Westerweel & Scarano, 2005).

2.3 Numerical model

Three-dimensional Large Eddy Simulations (OpenFOAM v2.3.0) of flow through emergent vegetation using the numerical methodology of Etminan et al. (2018) were employed in this study. A detailed description can be found in Etminan et al. (2017, 2018), and therefore, only a summary is provided herein. A set of four cylinders ($d = 0.01$ m) in a staggered arrangement was used to represent emergent vegetation. To simulate an infinite array of cylinders, cyclic boundary conditions were imposed in the streamwise and spanwise directions of the computational domain, formed by four sets of an O-grid block and a Cartesian H-grid block (refer to Figure 2 in Etminan et al. (2018)). In addition, a no-slip condition was imposed around each cylinder and at the bed. The data was only collected after 15 flow-through periods to ensure a fully-developed flow condition.

The ratio between the diameter of, and distance between, the elements was varied to achieve canopy densities ranging from $\phi = 0.016 - 0.25$ (Table 2). For each density, three flow conditions (based on the pore velocity, U_p) were tested; this velocity is defined as that averaged over the fluid space (Tanino & Nepf, 2008b) and can be calculated as $Q/WH(1-\phi)$, equivalent to $U_p = U_b/(1-\phi)$. Time-averaged flow parameters were evaluated across a minimum period of 45 flow-through periods.

252 **Table 2. Numerical simulation conditions**

Density, ϕ	Frontal area, a [m^{-1}]	Pore velocity, U_p [m/s]
0.016	2.0	0.05, 0.10, 0.13
0.04	5.1	
0.08	10.2	
0.12	15.3	
0.20	25.5	
0.25	32.0	

253 Previous studies have extensively validated the numerical model employed here for
254 emergent canopy flow (Etminan et al., 2017, 2018).

255 A comparison of the time-averaged streamwise velocity and turbulence intensity profiles
256 against experimental data reported by Liu et al. (2008) at five locations within the array showed
257 that the model accurately reproduces the experimental profiles of streamwise velocity and
258 turbulence intensity at all five locations (as shown in Figure 3 of Etminan et al. (2017)). In addition,
259 to specifically investigate the capacity of the model to reproduce the near-bed flow structure,
260 numerical profiles of both viscous and Reynolds stresses in the near-bed region were compared
261 against experimental data reported in Yang et al. (2015). This comparison again yielded strong
262 agreement between numerical and experimental data ($R^2 = 0.95$ and 0.81 for viscous and
263 Reynolds stresses, respectively, Figure 3 in Etminan et al. (2018)).

264 **2.5 Parameter definitions and data analysis**

265 **2.5.1. Experimental data**

266 Traditionally, the boundary layer thickness is defined as the height above the boundary at
267 which the velocity reaches 99% of the free stream velocity (Nowell & Jumars, 1984). This
268 definition, however, cannot be easily applied in vegetated flows due to the generation of a
269 secondary flow pattern (velocity overshoot) at the base of the canopy elements (Figure 3a). In the
270 case of emergent vegetation, the velocity reaches a depth-uniform value some distance from the
271 bed (inset figure 3a). The local thickness of the BBL ($\tilde{\delta}$) is defined here as the height at which the
272 temporally-averaged velocity ($\bar{u}$) first reaches this value (Figure 3a). For the experimental data

presented in this paper, all spatially-averaged flow statistics are averages over transects 2, 3 and 4 (Figure 2b). In particular, the temporally- and spatially-averaged streamwise velocity ($\langle\bar{u}\rangle$) in the region $z/d > 4$ was always within 5% of the estimated pore velocity U_p (Figure 3b) across all runs. Additionally, $\langle\bar{u}\rangle$ at the top of the spatially-averaged BBL layer thickness ($z = \langle\tilde{\delta}\rangle$) can be approximated to U_p.

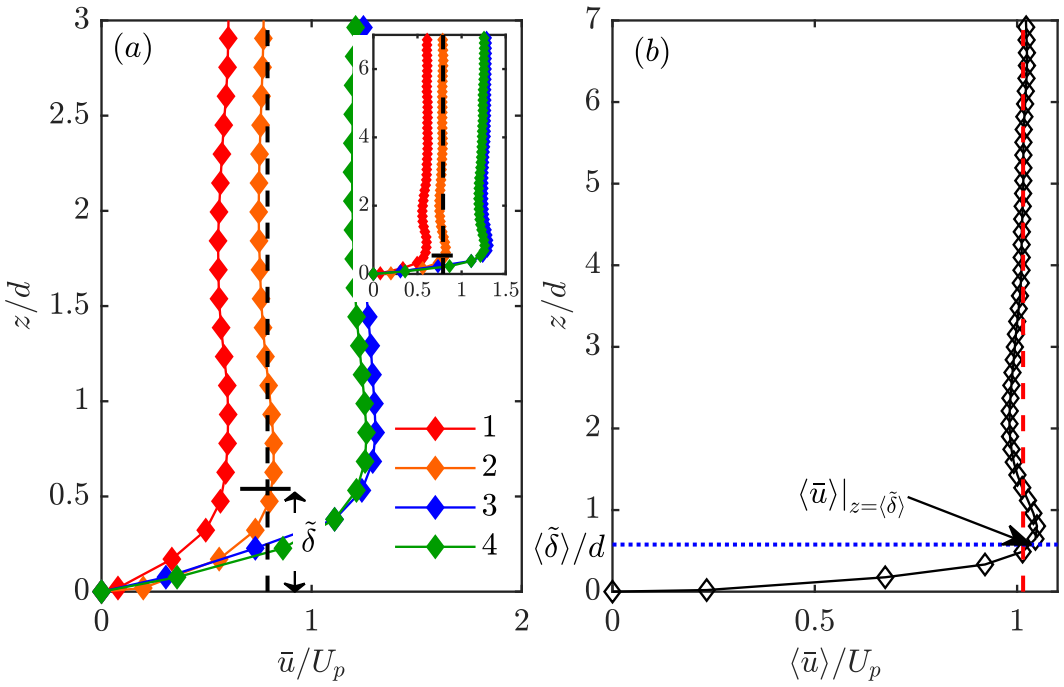

Figure 3. (a) Time-averaged streamwise velocity profiles normalized by the pore velocity (U_p) at a typical location on each of the measured transects (Figure 2b) from experimental data with $\phi = 0.025$ and $U_p = 0.065$ cm/s. The arrow indicates the BBL thickness ($\tilde{\delta}$) and the black dashed line represents the depth-uniform velocity. The inset shows an enlarged view. (b) The temporally- and spatially-averaged streamwise velocity ($\langle\bar{u}\rangle$) profile normalized by the pore velocity (U_p). The blue dashed line indicates the spatially-averaged BBL layer thickness ($\langle\tilde{\delta}\rangle$) and the red dashed line represents the depth-uniform velocity. The temporally- and spatially-averaged streamwise velocity at the top of $\langle\tilde{\delta}\rangle$ is within 5% the estimated pore velocity (arrow).

In all flows, the temporally- and spatially-averaged total stress ($\langle\bar{\tau}(z)\rangle$):

$$\langle\bar{\tau}(z)\rangle = \langle\rho\nu\frac{\partial\bar{u}}{\partial z}\rangle - \rho\langle\overline{u'w'}\rangle - \rho\langle\bar{u}''\bar{w}''\rangle, \quad (2)$$

At the bed ($z = 0$), for smooth and impermeable beds, the no-slip condition requires the second and third terms in (2) to be zero, such that $\langle\bar{\tau}\rangle|_{z=0} = \rho\nu \frac{\partial\langle\bar{u}\rangle}{\partial z}\Big|_{z=0}$; therefore, the spatially-averaged bed shear stress is simply:

$$\langle\bar{\tau}_b\rangle = \rho\nu \frac{\partial\langle\bar{u}\rangle}{\partial z}\Big|_{z=0}. \quad (3)$$

The temporally- and spatially-averaged turbulent kinetic energy is defined as:

$$\langle\bar{k_t}\rangle = 0.5\big(\langle\overline{u'^2}\rangle + \langle\overline{v'^2}\rangle + \langle\overline{w'^2}\rangle\big), \quad (4)$$

where u', v', and w' are the turbulent velocity fluctuations in streamwise, spanwise, and vertical directions, respectively. Given that the PIV measurements do not record the spanwise component of the velocity, we are forced to assume that $\overline{u'^2} \approx \overline{v'^2}$ (as in Tanino & Nepf (2008a)), such that the turbulent kinetic energy for emergent canopies can be approximated as:

$$\langle\bar{k_t}\rangle \approx 0.5\big(2\langle\overline{u'^2}\rangle + \langle\overline{w'^2}\rangle\big). \quad (5)$$

In this study, we will show the existence of a clear relationship between the BBL thickness and the near-bed TKE (section 3.2). Moreover, we will develop a TKE-based model for the BBL thickness and, ultimately, the bed shear stress (Section 4.1). Therefore, a predictive formulation for TKE is needed. Here, we employ the model of Tanino and Nepf (2008) for the turbulence intensity within an array of emergent cylinders:

$$\bar{k}_t = \gamma^2 \left(C_D \frac{l_t}{d} \frac{2\phi}{(1-\phi)\pi}\right)^{2/3} U_p^2, \quad (6)$$

In (6), γ is an empirical constant, C_D is the element drag coefficient, and it was estimated as $C_D = 1 + Re_c^{2/3}$, where $Re_c = (U_p d/\nu)((1-\phi)/(1-\sqrt{2\phi/\pi}))$ (Etminan et al., 2017). The eddy length-scale l_t is indicative of the scale associated with the mixing due to turbulent eddies (Tennekes & Lumley, 1972; Tanino & Nepf, 2008a).

2.5.2. Numerical data

To provide a statistical measure of the spatial variability of the velocities, total stress, and turbulent kinetic energy within the BBL for different canopy densities and flow conditions, the ratio between the RMS value ($\bar{\zeta}_{RMS}$) and the temporally- and spatially-averaged value ($\langle\bar{\zeta}\rangle$) was

calculated for all numerical runs. Given the full 3D spatial coverage of the LES simulations, robust estimates of spatially-averaged quantities can be obtained from the numerical model. Furthermore, all three components of the TKE could be measured directly, as per Eq. (4). For a given flow variable (ζ), the horizontally-averaged root-mean-squared (RMS) value (ζ_{RMS}) is calculated as

$$\zeta_{RMS}(z) = \sqrt{\frac{1}{n}\sum[\bar{\zeta}(x,y,z) - \langle\bar{\zeta}\rangle(z)]^2}, \quad (7)$$

where $\bar{\zeta}$ is the temporally-averaged value, $\langle\bar{\zeta}\rangle$ is the temporally- and spatially-averaged value, and n is the number of elements used in the sum. Flow statistics recorded in the region immediately adjacent to the cylinders (see figure 4 for further detail) were excluded from calculations of spatial averages as they are not representative of values at the canopy scale. The diameter of this excluded area (d_{exc}) was defined in Etminan et al. (2018) and is reported in Table 3.

Table 3. Excluded area diameter of the circle around the elements.

Density, ϕ	**Diameter of the excluded area, d_{exc}/d**
0.016	2.5
0.04	2.5
0.08	2.0
0.12	1.8
0.20	1.6
0.25	1.6

Finally, the mean absolute percentage deviation (M) was calculated to identify single-point locations that most closely match the spatial average value of the flow characteristics for a staggered-ordered emergent array of canopies:

$$M(x,y) = \frac{100}{m}\sum_{1}^{m}\left|\frac{\bar{\zeta}(x,y,z) - \langle\bar{\zeta}\rangle(z)}{\langle\bar{\zeta}\rangle(z)}\right|, \quad (8)$$

where m is the number of vertical values used in the sum.

3 Results

3.1 Horizontal variability of the flow characteristics within the BBL

Direct local estimates of near-bed flow characteristics from numerical simulations show variations of the same order as the temporally and spatially averaged values, revealing the high spatial variability at the element scale (Figure 4). The highest values of BBL thickness ($\tilde{\delta}(x,y)$) and temporally averaged streamwise velocity ($\bar{u}(x,y)$) are mostly confined to the area between element rows, whereas the smallest values are found in the element wakes (Figure 4a,b). Such regions of diminished and elevated velocities are a direct consequence of the sheltering and channelling effect produced by the canopy elements. Conversely, the highest values of local turbulent kinetic energy ($\bar{k}_t(x,y)$) are found in cylinder wakes with the smallest values in the channel between rows (Figure 4c). This variability indicates the major influence of element wakes on local values of $\bar{k}_t$ and, ultimately, on the temporally- and spatially-averaged value ($\langle\bar{k}_t\rangle$).

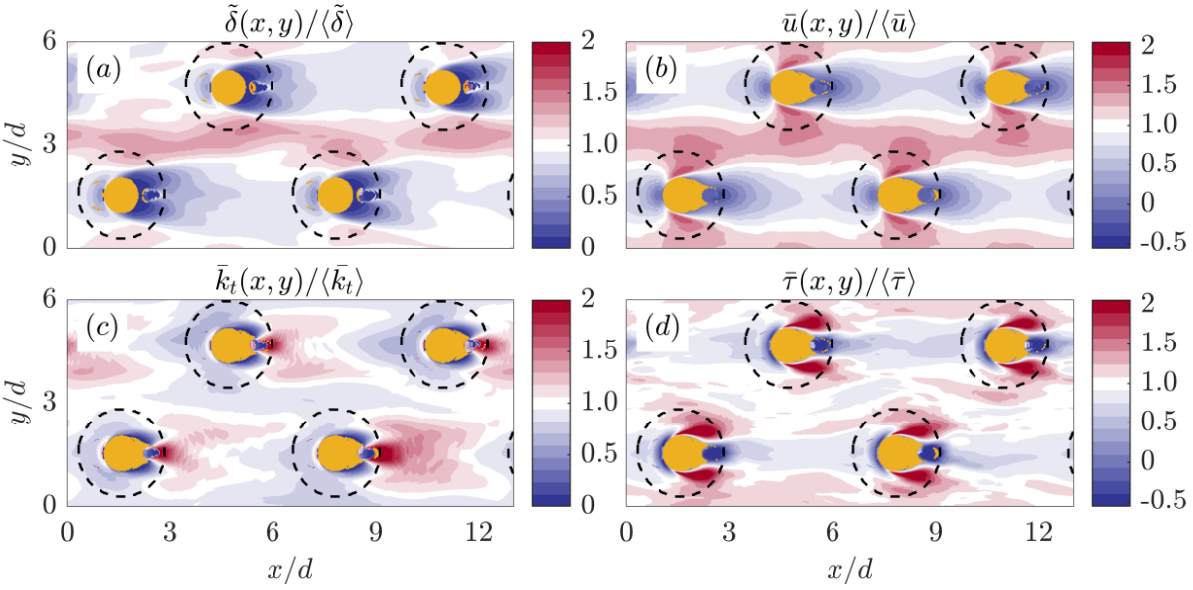

Figure 4. Horizontal variability of the dimensionless (a) BBL thickness, along with (b) streamwise velocity; (c) turbulent kinetic energy and (d) total stress, all vertically-averaged over the local BBL thickness $\tilde{\delta}(x,y)$ for the numerical case with $Re_{p,d} = 500$ and density $\phi = 0.04$. The flow is from left to right. The dashed line represents the area excluded from horizontal average calculations. Over a scale of an element diameter, variations of more than twice the temporally- and spatially- averaged value can be observed in near-bed flow characteristics, indicating the significant horizontal variability of flow through emergent vegetation. As negative values of streamwise velocity and total stress are possible, the lower limit of the colour bar differs between panels.

The horizontal variability of the total stress reveals areas of extreme stress ($\bar{\tau}(x,y)/\langle\bar{\tau}\rangle \gg 2$) on the sides of the cylinders (Figure 4d). These areas of enhanced stress are mainly generated by the compression of streamlines around canopy elements. Moreover, local values of negative stresses can be observed in the areas directly upstream and downstream of the cylinders. Regions of negative stress have been previously observed around individual cylinders, and they are linked to the development of horseshoe vortices (upstream region) and flow recirculation in the wake region (downstream region) (Schanderl et al., 2017). Further evidence of flow recirculation in the wake is seen in negative values of streamwise immediately downstream of the cylinders (Figure 4b).

Additionally, far from the region adjacent to the cylinders (outside the dashed line circle), the local stress values in the middle channel are close to the spatially-averaged value, and areas of reduced stress are observed in the cylinder wakes (white and blue colour in Figure 4d). The maps of near-bed flow characteristics in Figure 4 allow clear spatial correlations to be identified. For instance, locations of BBL thickness and streamwise velocity are positively correlated, whereas locations of BBL thickness and TKE are negatively correlated. The observed interplay between these variables indicates the possible impact of the streamwise velocity and near-bed TKE in controlling the BBL thickness, which we address in the next section.

The influence of canopy density and Reynolds number (defined as $Re_{p,d} = U_p d/\nu$) in the horizontal variability of near-bed flow characteristics is presented in Figure 5. Monotonical increases in RMS values of bottom boundary layer thickness, streamwise velocity and total stress (normalized by the temporally- and spatially-averaged values) are observed with canopy density (Figure 5a,b,d). This increase in horizontal variability with density is generated by stronger channelling and sheltering effects in denser vegetation, confirming that the element configuration largely controls spatial variability of the near-bed flow characteristics. In contrast, the horizontal variability of near-bed TKE decreases with canopy density (Figure 5c). This decrease in dense canopies results from an overall increment of the wake turbulence produced by the larger number of elements per unit area.

Finally, the magnitude of normalised RMS values of near-bed flow characteristics (visualised in Figure 4, quantified in Figure 5) highlights the difficulties associated with

understanding near-bed hydrodynamic processes from single-point observations. Numerical models that can resolve this variability, or at the very least provide an indication of the measurement locations required to capture it, are helpful tools in understanding spatial variation in the near-bed flow and have been employed here.

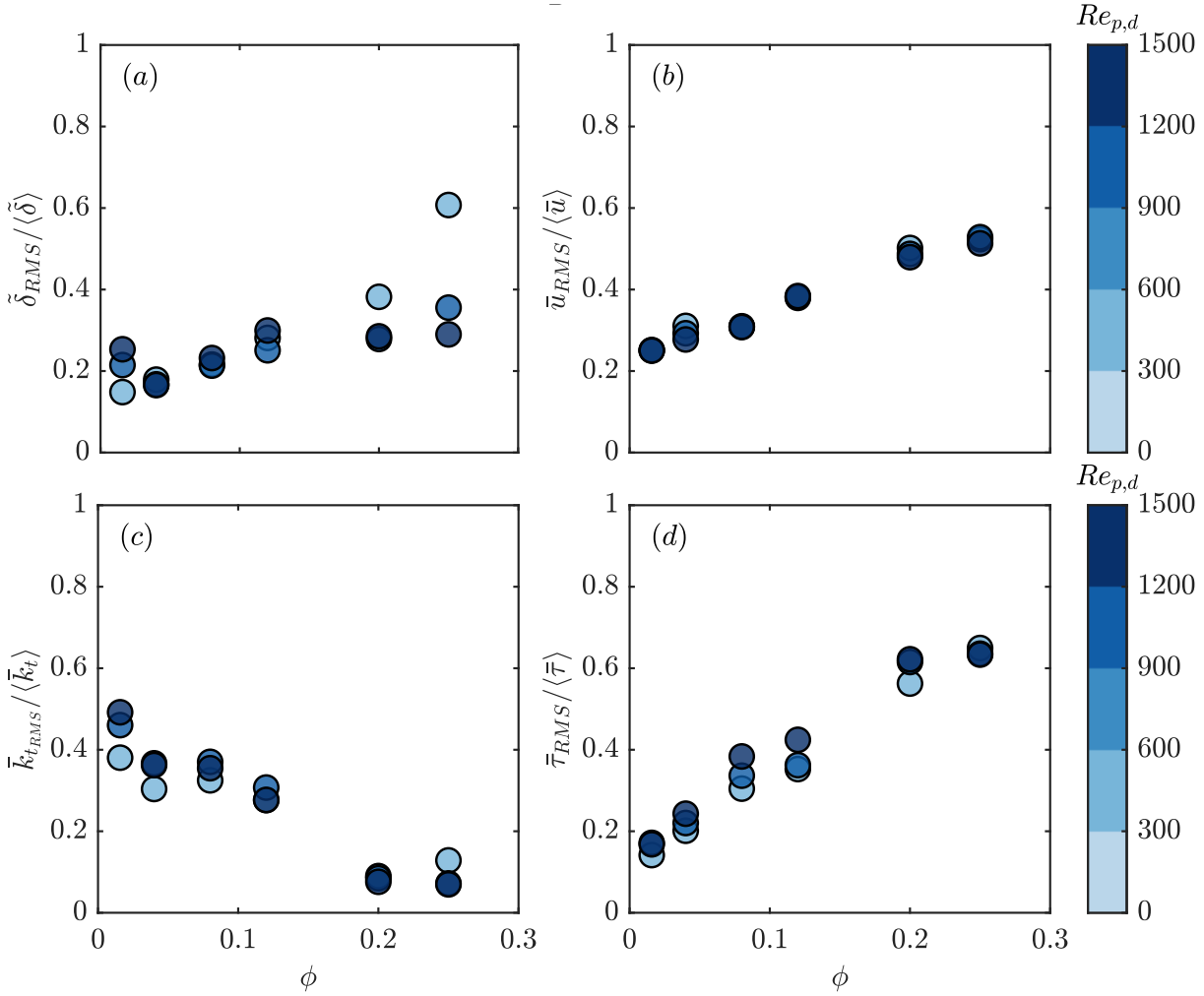

Figure 5. The ratio between the horizontally-averaged RMS values and the temporally- and spatially-averaged values of (a) boundary layer thickness, (b) streamwise velocity, (c) turbulent kinetic energy, and d) total stress. The canopy density largely controls the horizontal variability of the near-bed flow characteristics.

3.2 The bottom boundary layer thickness

In this section, experimental and numerical data are integrated to quantify the thickness of the bottom boundary layer across different canopy densities and highlight how turbulence levels regulate this thickness. Bottom boundary layer thickness with different canopy and flow properties

showed that this layer is primarily controlled by the canopy density (decreasing on denser canopies) and the element diameter (Figure 6a). This result is consistent with previous observations of the linear-stress region (a sublayer within the BBL) decreasing with canopy density (Yang et al., 2015; Etminan et al., 2018). The Reynolds number has a secondary influence on the BBL thickness (BBL thickness decrease with Reynolds number), but it is generally minor compared to the impact of the canopy density. It can be observed from Figure 6a that as the canopy density increases, the boundary layer thickness becomes less sensitive to changes in density. Conversely, the dimensionless spatially-averaged TKE ($\langle \bar{k}_t \rangle / \langle \bar{u} \rangle^2$) monotonically increases with canopy density (Figure 6b), as a result of the increase in wake turbulence produced by a larger number of cylinders per unit area.

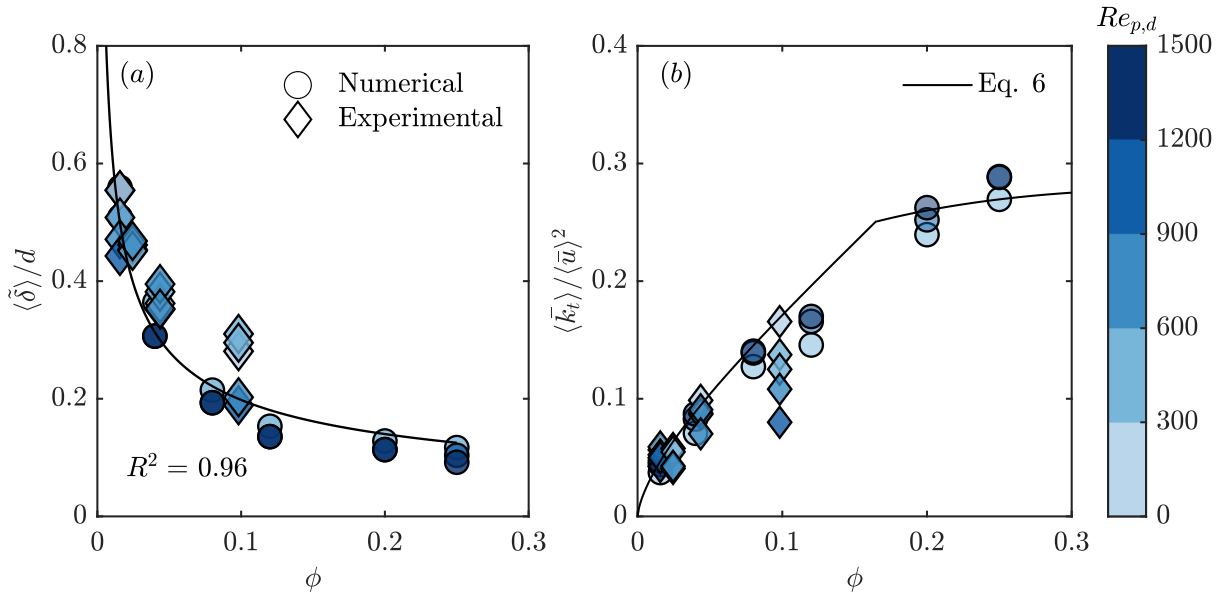

Figure 6. (a) The strong correlation between the dimensionless spatially-averaged BBL thickness ($\langle \tilde{\delta} \rangle / d$) and the canopy density (ϕ). There is strong agreement between numerical and experimental estimates of BBL thickness. The solid line represents the line of best fit, $\langle \tilde{\delta} \rangle / d = 0.06/\phi^{0.5}$. (b) variation of dimensionless spatially-averaged turbulence intensity $\langle \bar{k}_t \rangle / \langle \bar{u} \rangle^2$with the canopy density for the experimental and numerical data. The solid black line represents the curve given by Eq. 6.

As suggested in Figure 6, there is a strong negative correlation between the dimensionless spatially-averaged thickness of the BBL and the dimensionless temporally- and spatially-averaged turbulent kinetic energy at the top of the BBL ($z = \langle \tilde{\delta} \rangle$) (Figure 7). This relationship takes the form

411
$$\frac{\langle\tilde{\delta}\rangle}{d} = 0.022\,\frac{\langle\bar{u}\rangle^2}{\langle\bar{k}_t\rangle}\bigg|_{z\,=\,\langle\tilde{\delta}\rangle} \quad . \tag{9}$$

412

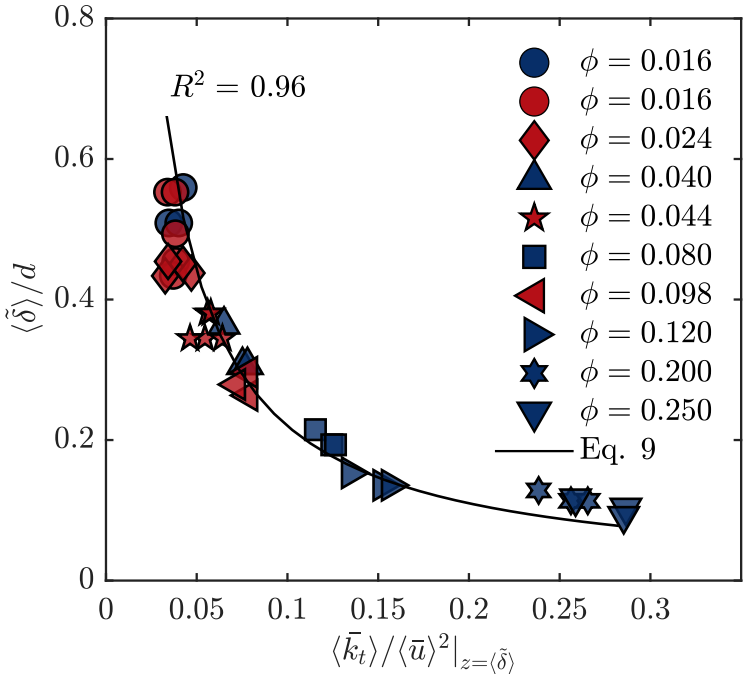

413

414 Figure 7. The inversely proportional relationship between the dimensionless spatially-averaged BBL
415 thickness ($\langle\tilde{\delta}\rangle/d$) and dimensionless TKE ($\langle\bar{k}_t\rangle/\langle\bar{u}\rangle^2$) at the top of the bottom boundary layer. The blue markers
416 represent numerical data and the red markers experimental data. The solid black line represents the best fit curve given
417 by Eq. 9. The inversely proportional relationship supports the notion of a direct influence of the TKE on the thickness
418 of the BBL for the spatially-averaged values.

419 In addition to the correlation between spatially-averaged values, there is a strong spatial
420 correlation between BBL thickness and near-bed TKE within a given canopy (Figure 8). Notably,
421 even though there is some scatter, most of the locally-measured data (red patches) follow the trends
422 of the spatially-averaged value (the line in Figure 8, shown in Eq. 9).

423 The inversely proportional relationship of boundary layer thickness and turbulence
424 intensity with canopy density suggests the possibility of a causal link between these two variables,
425 where the increase in the vertical moment transport generated by the 'external' turbulence from
426 the plants creates a thinner boundary layer. It is noteworthy that within each patch, where the
427 density is not changing, the local values of BBL thickness and the near-bed TKE have an inverse

relationship within a given flow, i.e., local values of high TKE generates a thinner local BBL. This observed local agreement further indicates a causal link between near-bed TKE and BBL thickness.

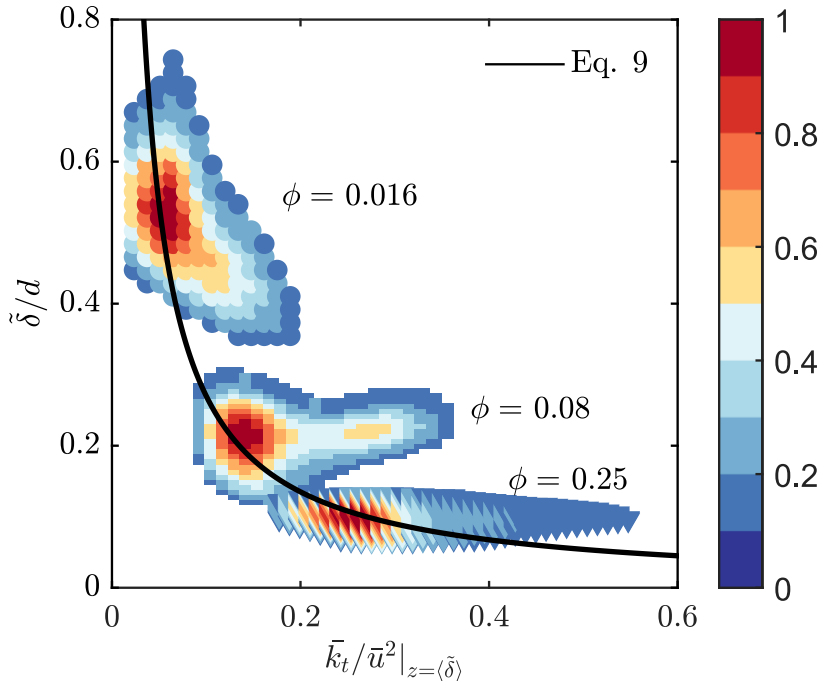

Figure 8. Local values of dimensionless bottom boundary layer thickness as a function of the dimensionless turbulent kinetic energy (evaluated at the top of the BBL) for three canopy densities $= 0.016$, $\phi = 0.08$, $\phi = 0.25$ and $Re_{p,d} = 500$. The solid black line represents the best fit curve given by Eq. 9. The colour bar indicates the data density normalized by the total data in the domain.

3.3 Vertical structure of stresses within BBL

The significant spatial variability of the near-bed flow characteristics (Figure 4) indicates that dispersive stresses may contribute significantly to momentum transport in the near-bed region. The vertical structure of the stress components (terms *i*, *ii* and *iii* in Eq. 1) and the total shear stress within the BBL are presented in Figure 9 for a flow through a canopy with a density of 0.04. This vertical structure defines three important sublayers within the BBL. In the sublayer closest to the bed, $z \lesssim \langle\tilde{\delta}\rangle/4$ (ranging from 0.25-1.5 mm in this study), the viscous stress is the dominant component of the total shear stress, and the Reynolds and dispersive stresses are both negligible. The second sublayer, in which all three stress components are significant, lies between $\langle\tilde{\delta}\rangle/4$ and

446 $3\langle\tilde{\delta}\rangle/4$. Finally, within the third sublayer $3\langle\tilde{\delta}\rangle/4 \lesssim z \lesssim \langle\tilde{\delta}\rangle$, the dispersive and Reynolds stresses
447 dominate. Note that this vertical structure of the normalized stresses within the bottom boundary
448 layer was qualitatively similar in shape across all densities and flows. Of particular significance is
449 that the BBL in emergent canopies is a region of roughly constant total shear stress related to the
450 bed shear stress.

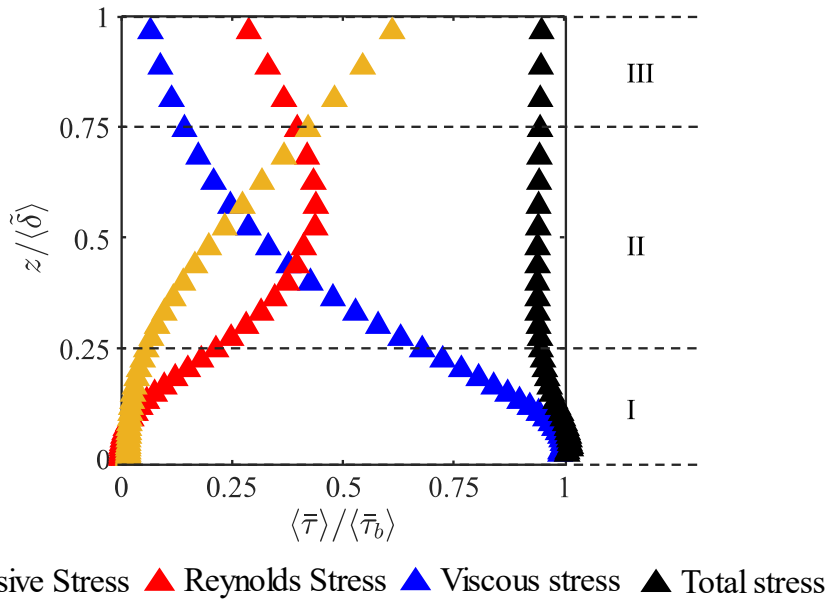

451

452 Figure 9. Vertical structure of spatially averaged stress components within the BBL for the numerical case
453 with density $\phi = 0.04$ and $Re_{p,d} = 500$ (for which $\langle\tilde{\delta}\rangle = 0.34$ cm). Stress components have been normalized by $\langle\bar{\tau}_b\rangle$,
454 the value at the bed (z = 0). Roman numerals define three important sublayers across the BBL. Although the
455 contributions of the components vary with height above the bed, the BBL in emergent canopies is seen to be a region
456 of approximately constant shear stress.

457 The vertical variation of the stress components emphasises the fact that direct
458 measurements of bed shear stress require either velocity gradient measurements within the region
459 adjacent to the bed (Region I) or measurements across the horizontal plane to accurately capture
460 the dispersive stresses. Either requirement is likely to prove impractical in experimental studies.
461 Therefore, we propose a simple scaling approach to estimate the spatially-averaged bed shear
462 stress in emergent canopies. Assuming self-similarity of the velocity profile in the BBL, the
463 velocity gradient at the bed scales upon $\bar{u}|_{z=\tilde{\delta}}/\tilde{\delta}$ and therefore, it is possible to approximate the
464 temporally- and spatially- averaged bed shear stress (Eq. 3) as:

$$\langle \bar{\tau}_b \rangle = \mu \left. \frac{\partial \langle \bar{u} \rangle}{\partial z} \right|_{z=0} \sim \mu \frac{\langle \bar{u} \rangle|_{z=\langle \tilde{\delta} \rangle}}{\langle \tilde{\delta} \rangle}. \quad (10)$$

There is a strong agreement ($R^2 = 0.89$) between measured bed shear stresses and those predicted by the scaling relationship in Eq. 10 (Figure 10). This strong agreement supports the self-similarity assumption of the mean velocity profile in the BBL as well as the validity of Eq. 10 in predicting bed shear stress in aquatic vegetation. Despite the strong agreement, the model underestimates the bed shear stress at low canopy densities ($\phi < 0.04$) and high Reynolds numbers ($Re_{p,d}$>1000). Ultimately, the validity of Eq. 10 depends upon a self-similarity of mean velocity profiles in the BBL of vegetated flows, a self-similarity which appears to break down at low canopy density and high Reynolds numbers. Thus, this underestimation can be explained by, at low density and high Reynolds number, there is a reduced impact of the vegetation on the mean velocity structure; in the limit of zero density, the vertical velocity gradient will tend towards that observed in flow over a bare bed. Indeed, in low-density canopies, the thicknesses of the viscous-stress-dominated sublayer (Layer I in Figure 9) in vegetated (H_{v}) and unvegetated ($H_{\mathrm{v,unveg}}$) beds are equivalent (Yang et al., 2015). The scaling relationship in Eq. 10 was modified to reflect this change in velocity structure at low canopy density:

$$\langle \bar{\tau}_b \rangle = \mu \left. \frac{\partial \langle \bar{u} \rangle}{\partial z} \right|_{z=0} \sim \mu \frac{\langle \bar{u} \rangle|_{z=\tilde{\delta}_e}}{\tilde{\delta}_e}, \quad (11)$$

where $\tilde{\delta}_e$ is the effective BBL thickness given by $\tilde{\delta}_e = \min(\langle \tilde{\delta} \rangle, H_{\mathrm{v,unveg}})$ with $H_{\mathrm{v,unveg}}$ taken as $25\nu/\langle \bar{u}_* \rangle$, as for bare channel flows, $H_{\mathrm{v,unveg}} \langle \bar{u}_* \rangle \backslash \nu$ =25 (see Figure 2 in Yang et al., 2015). When considering the effective BBL thickness as the length scale that governs the velocity gradient at the bed (i.e. Eq. 11), the prediction of bed shear improves significantly ($R^2 = 0.96$, Figure 10b).

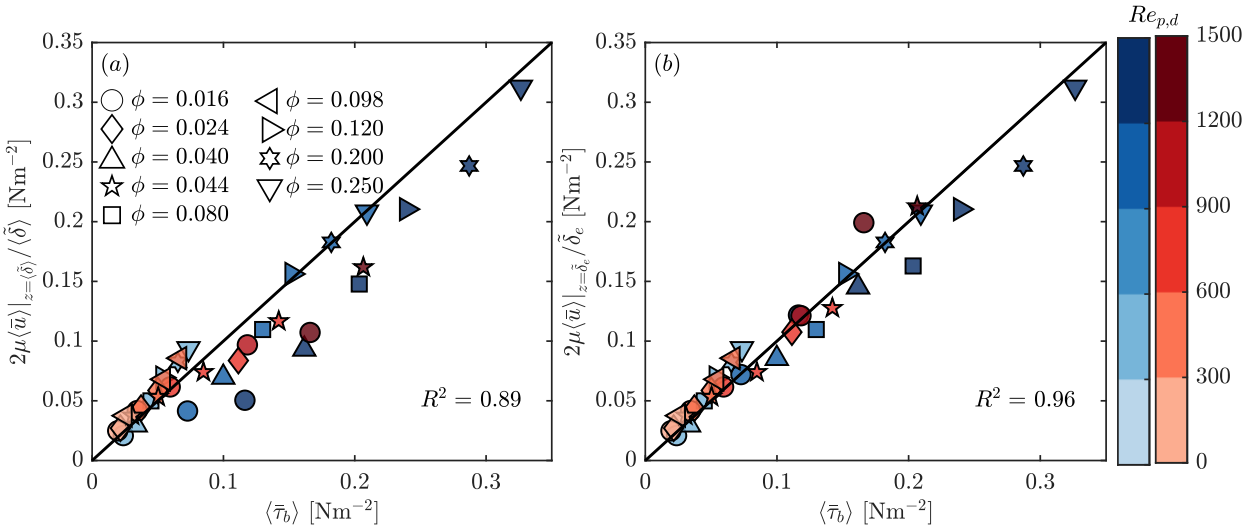

Figure 10. Agreement between measured bed shear stresses and those predicted by the scaling relationship in (a) Eq.10, the solid line represents the linear fit $\langle\bar{\tau}_b\rangle = 2.0\mu\langle\bar{u}\rangle|_{z=\langle\tilde{\delta}\rangle}/\langle\tilde{\delta}\rangle$, and (b) Eq. 11, the solid line represents the linear fit $\langle\bar{\tau}_b\rangle = 2.0\mu\langle\bar{u}\rangle|_{z=\tilde{\delta}_e}/\tilde{\delta}_e$. The blue markers represent the numerical data, and the red markers represent experimental data. The blue and red colour bar indicates the $Re_{p,d}$ for numerical and experimental data, respectively.

4. Discussion

4.1. Developing a predictive model of bed shear stress

Given the high correlation between $\langle\bar{\tau}_b\rangle$ and $\mu\langle\bar{u}\rangle|_{z=\tilde{\delta}_e}/\tilde{\delta}_e$ (Figure 10b), a model to predict the bed shear stress can be obtained from Eq.11. Defining the friction velocity $\langle\bar{u}_*\rangle$ through $\langle\bar{\tau}_b\rangle = \rho\langle\bar{u}_*\rangle^2$, and substituting $\langle\bar{u}\rangle|_{z=\tilde{\delta}_e} = U_p$ and $\tilde{\delta}_e = \min(\langle\tilde{\delta}\rangle, H_{\mathrm{v,unveg}})$ into Eq. 11, a model for friction velocity ($\langle\bar{u}_*\rangle_{mod}$) can be written as $\langle\bar{u}_*\rangle_{mod} = \max\left(\sqrt{2\nu U_p/\langle\tilde{\delta}\rangle}, \sqrt{2\nu U_p/H_{\mathrm{v,unveg}}}\right)$. Using the TKE-dependent relationship for BBL thickness in Eq. 9, $\sqrt{2\nu U_p/\langle\tilde{\delta}\rangle}$ can be rewritten as:

$$C\sqrt{\frac{\langle\bar{k}_t\rangle|_{z=\langle\tilde{\delta}\rangle}}{Re_{p,d}}}, \tag{12}$$

with $C = 8$. Furthermore, by characterising $H_{\mathrm{v,unveg}}$ in terms of a bed drag coefficient, C_f (defined as $\langle\bar{u}_*\rangle^2/U_p^2$), such as $H_{\mathrm{v,unveg}} = 2\nu/C_f U_p$, we can express $\sqrt{2\nu U_p/H_{\mathrm{v,unveg}}}$ as:

501 $$\sqrt{C_f}U_p. \quad (13)$$

502 Therefore, the model for the friction velocity becomes

503 $$\langle \bar{u}_* \rangle_{mod} = \max\left(C\sqrt{\frac{\langle \bar{k}_t \rangle|_{z=\langle \tilde{\delta} \rangle}}{Re_{p,d}}}, \sqrt{C_f}U_p \right). \quad (14)$$

504 This model (Eq. 14) requires *a priori* knowledge of the temporally- and spatially-averaged TKE
505 at the top of the BBL $\left(\langle \bar{k}_t \rangle|_{z\,=\,\langle \tilde{\delta} \rangle}\right)$ and the bed drag coefficient (C_f). The model for predicting
506 TKE in Eq. 6 can be employed here for estimating $\langle \bar{k}_t \rangle|_{z=\langle \tilde{\delta} \rangle}$; if we assumed Eq 6 to be valid at
507 every vertical position (as in Xu & Nepf (2020)), then

508 $$\langle \bar{k}_t \rangle|_{z=\langle \tilde{\delta} \rangle} = \gamma^2 \left(C_d \frac{\langle l_t \rangle}{d} \frac{2\phi}{(1-\phi)\pi} \right)^{2/3} \langle \bar{u} \rangle|^2_{z=\langle \tilde{\delta} \rangle}. \quad (15)$$

509 Given the wide range of densities in this study, the characteristic eddy length scale (l_t) depends on
510 the ratio of element diameter (d) to element spacing (s_n). Following Tanino & Nepf (2008), we
511 used a length scale of $\langle l_t \rangle = d$ for $d/s_n < 0.53$ and $\langle l_t \rangle = s_n$ for $d/s_n \geq 0.53$. The velocity at
512 the top of the BBL $\langle \bar{u} \rangle|_{z=\langle \tilde{\delta} \rangle}$ was replaced by the cross-sectional average fluid velocity, U_p (Figure
513 3b) The empirical coefficient γ^2 in Eq. 15 was estimated from the least-squares fitting between
514 $\langle \bar{k}_t \rangle|_{z=\langle \tilde{\delta} \rangle}$ and $\gamma^2 \left(C_d \frac{\langle l_t \rangle}{d} \frac{2\phi}{(1-\phi)\pi} \right)^{2/3} \langle \bar{u} \rangle|^2_{z=\langle \tilde{\delta} \rangle}$ using both experimental and numerical data (Figure
515 11).

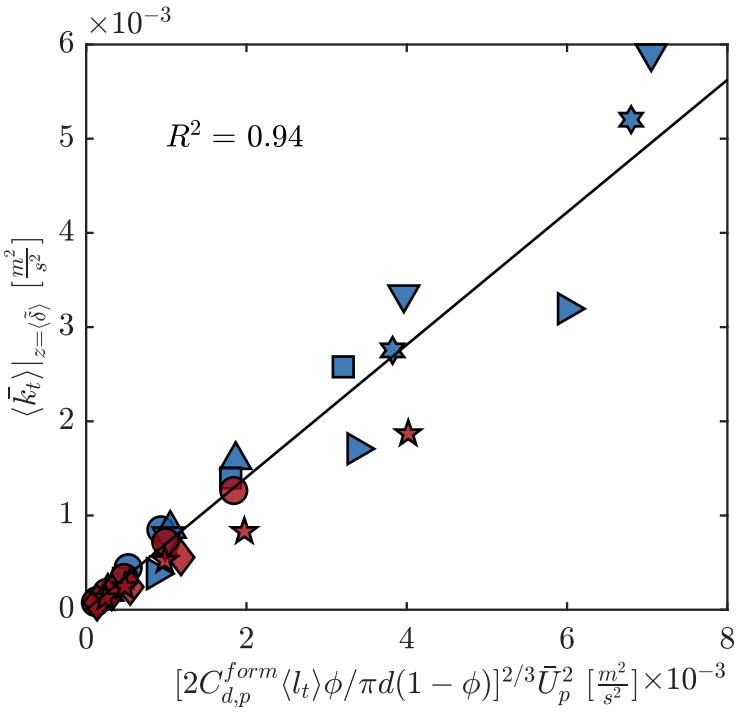

Figure 11. Least-squares fitting between the measured value of TKE at the top of BBL vs that predicted by Eqn. 13. The solid black line represents the line of best fit given by $y = \gamma^2 x$ with $\gamma^2 = 0.70$. Markers are as in Figure 7.

The bed drag coefficient required in Eq. 14 was found using the relation for $H_{\mathrm{v,unveg}}$ ($H_{\mathrm{v,unveg}}\langle \bar{u}_* \rangle \backslash \nu$ =25) found by Yang et al. (2015), leading to

$$C_f = \frac{2\nu}{H_{\mathrm{v,unveg}} U_p} = 0.08 \frac{\langle \bar{u}_* \rangle}{U_p}. \quad (16)$$

Since by definition $C_f = \langle \bar{u}_* \rangle^2 / U_p^2$, it must therefore take a value of approximately 0.0064. Substituting $\langle \bar{k}_t \rangle|_{z=\langle \tilde{\delta} \rangle}$, C_f, $Re_{p,d}$ and U_p in Eq.14, the agreement between the measured $\langle \bar{u}_* \rangle$ and modelled friction velocities ($\langle \bar{u}_* \rangle_{mod}$) is shown in figure 12. The strong agreement (R^2 = 0.90) between measured and modelled (Eq. 14) values of friction velocity (Figure 12) demonstrates the robust predictive capacity of the model, which only requires bulk properties of the system (i.e., the pore velocity, the canopy density and the bed drag coefficient) as inputs.

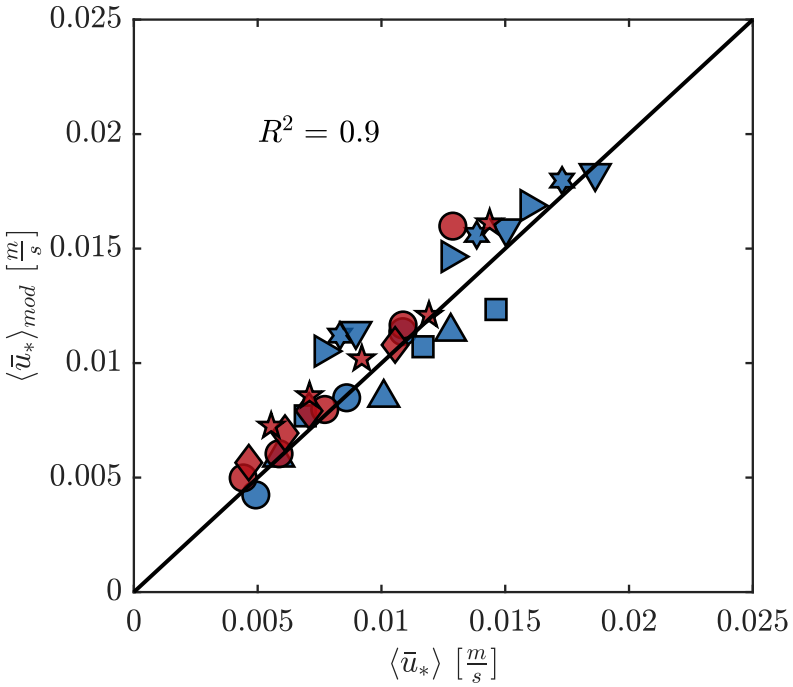

Figure 12. Comparison between measured spatially-averaged values of friction velocity with those predicted from Eq. 14 ($\langle \bar{u}_* \rangle_{mod}$). The solid line represents perfect agreement. Markers are as in Figure 7.

4.2. Implications for interpreting experimental measurements of flow properties

Given the significant spatial variability of near-bed flow characteristics in vegetation canopies, it is paramount to identify the locations that can be targeted in experimental studies to provide representative values of the spatially-averaged values. The horizontal locations where the mean absolute percentage deviation (M, Eqn. (8)) for streamwise velocity ($\bar{u}$), turbulent kinetic energy ($\overline{k_t}$) and total stress ($\bar{\tau}$) is less than 5% within the BBL are shown in Figure 13.

The horizontal distributions of $\bar{u}$, $\overline{k_t}$ and $\bar{\tau}$ show that the regions with significant deviations from spatial means (white regions in Figure 13) are concentrated around the wakes of the elements and are found to vary significantly with canopy density. As the density increases, these regions become narrower (relative to S/d), mainly due to the intensification of the flow channelling created by a staggered-ordered canopy model, along with the more complex wake interactions produced in dense canopies. Furthermore, in the near-bed region, the average deviation from spatially-averaged values ($M > 5\%$) across the total plan area for the bed shear stress is enhanced due to the strong interaction of the flow with the bed. As in this region, the local changes of near-

548 bed TKE induce changes in the BBL thickness (Figure 8), which in turn generates strong spatial
549 variability of bed shear stress.

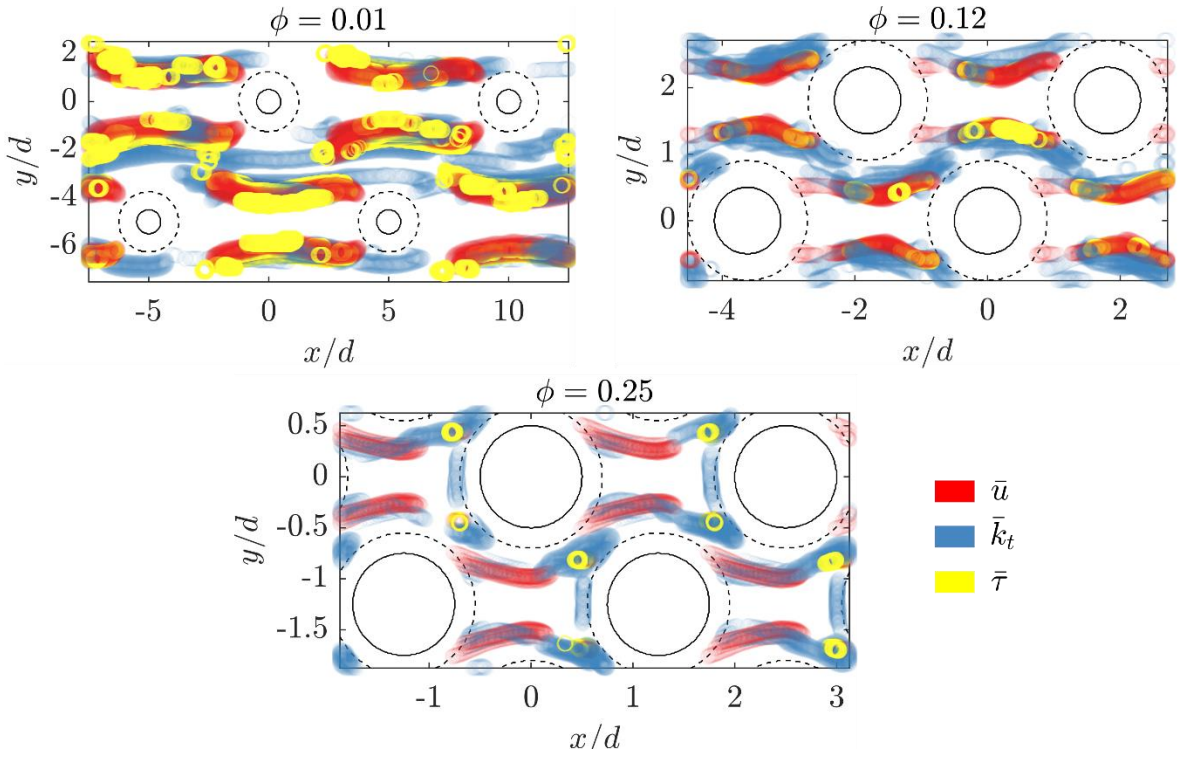

550

551 Figure 13. Horizontal distribution of locations with $M \leq 5\%$ for the streamwise velocity, $\bar{u}$ (red markers),
552 the turbulent kinetic energy, $\bar{k}_t$ (blue markers) and the total stress, $\bar{\tau}$ (yellow markers) within the BBL ($z \leq \langle\bar{\delta}\rangle$) for
553 three canopy densities. The dashed circle around the cylinders represents the excluded area for all the statistics.
554 Spatially representative statistics can be obtained in the region encompassed by a measurement volume that extends
555 from one side of an upstream cylinder to the same side of a downstream cylinder in the same row.

556 While the previous maps of *M* suggest the existence of local preferred measurement regions
557 (low values of *M*), we caution that their generalization to more heterogeneous and complex
558 canopies requires further research to understand the spatial variability of the flow characteristic.
559

560 **4.3 Implications for predicting sediment transport**

561 Current models can use either stress or TKE as an assumed driver of sediment motion &
562 transport. On the one hand, models based on TKE as the main driver of sediment transport (e.g.
563 Tinoco & Coco, 2014, 2016, 2018; Yang et al., 2016; Yang & Nepf, 2018, 2019) suggest that bed
564 shear stress-based sediment transport models (developed for bare beds) fail within vegetated
565 regions because they do not account for the vegetation generated turbulence. In other words, the

566 'external' turbulence from the plants and the bed shear stress are decoupled in these flows.
567 However, our results (Figures 7, 8 and 12) indicate the opposite, i.e., higher values of vegetated
568 generated TKE create a thinner BBL thickness, which in turn increases the bed shear stress. The
569 strong link between the bed shear stress and the near-bed TKE may explain why predictive models
570 using TKE are seen to excel in predicting sediment transport in vegetation canopies. On the other
571 hand, previous approaches based on predicting the thickness of the viscous-stress dominated
572 sublayer within the BBL (e.g. Nepf, 2012b; Yang et al., 2015) have taken it to be proportional to
573 the element diameter, d, such that $\bar{\tau} = \mu U/d$, (with U the depth-averaged velocity). As a result,
574 these models are unable to capture a dependence of boundary layer thickness on canopy density.
575 The results of this study suggest, however, that for constant element diameter, both the viscous
576 sublayer and the total BBL thickness vary significantly with canopy density (Figure 6), which may
577 be one reason why robust sediment transport predictions for vegetation canopies using the bed
578 shear stress have proven elusive.

579 In section 4.1 (Eq.14), a new method (validated in Figure 12) is proposed to estimate bed
580 shear stresses in emergent canopies based on the thickness of the boundary layer, the bed drag
581 coefficient and the temporally- and spatially-averaged velocity. This model incorporates the effect
582 of the near-bed TKE on the bed shear stress. Notably, the model presented in this study (Eq.14)
583 represents an alternative method for bed shear stress prediction, without requiring high-resolution
584 flow measurements near the bed, by directly linking the bed shear stress with the near-bed turbulent
585 kinetic energy. Finally, further research is needed to precisely assess the capacity of this model to
586 drive predictions of the onset of sediment motion and transport rates in vegetated environments.
587

588 **5 Conclusions**

589 Flows through emergent canopies are characterised by significant horizontal variability in
590 the thickness of the bottom boundary layer, velocities, stresses, and turbulent kinetic energy within
591 the layer. It is shown here that canopy density and element diameter control the boundary layer
592 thickness through its direct control of near-bed turbulent kinetic energy (TKE). Locally and in a
593 given flow, the near-bed turbulent kinetic energy (TKE) was negatively correlated with BBL
594 thickness across the studied flow conditions. Accordingly, a model for prediction of bed shear
595 stress is presented here that is based upon evaluation of this BBL thickness, and requires only

canopy density, bed drag coefficient and bulk velocity as further inputs. There is excellent agreement between model predictions and direct bed shear stress measurements in laboratory and numerical experiments. The link between 'external' turbulence from the plants, the BBL thickness, and ultimately the bed shear stress may explain why stress and TKE may be seen as drivers of sediment transport processes in vegetated flows.

6 Acknowledgments

This project forms part of a PhD study by M.C. at the University of Western Australia supported by the Commonwealth Government through an Australian Government Research Training Program Scholarship. Additional support was also provided by the Australian Research Council (Discovery Project DP200101545 and DP170100802).

7 References

Abdolahpour, M., Ghisalberti, M., McMahon, K., & Lavery, P. S. (2018). The impact of flexibility on flow, turbulence, and vertical mixing in coastal canopies. *Limnology and Oceanography*, *63*(6), 2777–2792. https://doi.org/10.1002/lno.11008

Beer, D. De, & Kühl, M. (2001). Interfacial microbial mats and biofilms. *The Benthic Boundary Layer*. https://doi.org/10.1128/AEM.70.11.6551

Cundy, A. B., Hopkinson, L., Lafite, R., Spencer, K., Taylor, J. A., Ouddane, B., et al. (2005). Heavy metal distribution and accumulation in two Spartina sp.-dominated macrotidal salt marshes from the Seine estuary (France) and the Medway estuary (U.K.). *Applied Geochemistry*, *20*(6), 1195–1208. https://doi.org/10.1016/j.apgeochem.2005.01.010

Etminan, V., Lowe, R., & Ghisalberti, M. (2017). A new model for predicting the drag exerted by vegetation canopies. *Water Resources Research*, *53*(4), 3179–3196. https://doi.org/10.1002/2016WR020090

Etminan, V., Ghisalberti, M., & Lowe, R. J. (2018). Predicting Bed Shear Stresses in Vegetated Channels. *Water Resources Research*, *54*(11), 9187–9206. https://doi.org/10.1029/2018WR022811

Grant, S. B., Gomez-Velez, J. D., & Ghisalberti, M. (2018). Modeling the Effects of Turbulence on Hyporheic Exchange and Local-to-Global Nutrient Processing in Streams. *Water Resources Research*. https://doi.org/10.1029/2018WR023078

Hemminga, M. A., & Duarte, C. M. (2000). Fauna associated with seagrass systems. In *Seagrass Ecology*

(pp. 199–247). Cambridge University Press. https://doi.org/10.1017/CBO9780511525551.007

Hooke, J. M. (2007). Monitoring morphological and vegetation changes and flow events in dryland river channels. *Environmental Monitoring and Assessment*, *127*(1–3), 445–457. https://doi.org/10.1007/S10661-006-9294-6

James, C. S., Jordanova, A. A., & Nicolson, C. R. (2002). Flume experiments and modelling of flow-sediment-vegetation interactions. *IAHS-AISH Publication*.

Jordanova, A. a., & James, C. S. (2003). Experimental Study of Bed Load Transport through Emergent Vegetation. *Journal of Hydraulic Engineering*, *129*(6), 474–478. https://doi.org/10.1061/(ASCE)0733-9429(2003)129:6(474)

van Katwijk, M. M., Bos, A. R., Hermus, D. C. R., & Suykerbuyk, W. (2010). Sediment modification by seagrass beds: Muddification and sandification induced by plant cover and environmental conditions. *Estuarine, Coastal and Shelf Science*, *89*(2), 175–181. https://doi.org/10.1016/J.ECSS.2010.06.008

Kothyari, U. C., Hashimoto, H., & Hayashi, K. (2009). Effect of tall vegetation on sediment transport by channel flows. *Journal of Hydraulic Research*, *47*(6), 700–710. https://doi.org/10.3826/jhr.2009.3317

Larsen, L. G., Harvey, J. W., & Crimaldi, J. P. (2009). Predicting bed shear stress and its role in sediment dynamics and restoration potential of the Everglades and other vegetated flow systems. *Ecological Engineering*, *35*(12), 1773–1785. https://doi.org/10.1016/j.ecoleng.2009.09.002

Liu, D., Diplas, P., Fairbanks, J. D., & Hodges, C. C. (2008). An experimental study of flow through rigid vegetation. *Journal of Geophysical Research: Earth Surface*, *113*(4), 1–16. https://doi.org/10.1029/2008JF001042

Lowe, R., Koseff, J. R., & Monismith, S. G. (2005). Oscillatory flow through submerged canopies: 1. Velocity structure. *Journal of Geophysical Research C: Oceans*, *110*(10), 1–17. https://doi.org/10.1029/2004JC002788

Lowe, R., Falter, J. L., Koseff, J. R., Monismith, S. G., & Atkinson, M. J. (2007). Spectral wave flow attenuation within submerged canopies: Implications for wave energy dissipation. *Journal of Geophysical Research*, *112*(C5), C05018. https://doi.org/10.1029/2006JC003605

Massel, S. R., Furukawa, K., & Brinkman, R. M. (1999). Surface wave propagation in mangrove forests. *Fluid Dynamics Research*, *24*(4), 219–249. https://doi.org/10.1016/S0169-5983(98)00024-0

Meinhart, C. D., Wereley, S. T., & Santiago, J. G. (2000). A piv algorithm for estimating time-averaged velocity fields. *Journal of Fluids Engineering, Transactions of the ASME*. https://doi.org/10.1115/1.483256

Morse, A. P., Gardiner, B. A., & Marshall, B. J. (2002). Mechanisms controlling turbulence development across a forest edge. *Boundary-Layer Meteorology*. https://doi.org/10.1023/A:1014507727784

Nepf, H. (1999). Drag, turbulence, and diffusion in flow through emergent vegetation. *Water Resources Research*, *35*(2), 479–489. https://doi.org/10.1029/1998WR900069

Nepf, H. (2012a). Flow and Transport in Regions with Aquatic Vegetation. *Annual Review of Fluid Mechanics*, *44*(1), 123–142. https://doi.org/10.1146/annurev-fluid-120710-101048

Nepf, H. (2012b). Hydrodynamics of vegetated channels. *Journal of Hydraulic Research, 50*(3), 262–279. https://doi.org/10.1080/00221686.2012.696559

Nepf, H., & Ghisalberti, M. (2008). Flow and transport in channels with submerged vegetation. *Acta Geophysica*, *56*(3), 753–777. https://doi.org/10.2478/s11600-008-0017-y

Nepf, H., & Vivoni, E. (2000). Flow structure in depth-limited, vegetated flow. *Journal of Geophysical Research: Oceans*, *105*(C12), 28547–28557. https://doi.org/10.1029/2000JC900145

Nikora, V., Goring, D., McEwan, I., & Griffiths, G. (2001). Spatially Averaged Open-Channel Flow over Rough Bed. *Journal of Hydraulic Engineering*, *127*(2), 123–133. https://doi.org/10.1061/(ASCE)0733-9429(2001)127:2(123)

Nobach, H., & Honkanen, M. (2005). Two-dimensional Gaussian regression for sub-pixel displacement estimation in particle image velocimetry or particle position estimation in particle tracking velocimetry. *Experiments in Fluids*. https://doi.org/10.1007/s00348-005-0942-3

Nowell, A. R. M. M., & Jumars, P. A. (1984). Flow Environments of Aquatic Benthos. *Annual Review of Ecology and Systematics*, *15*(1), 303–328. https://doi.org/10.1146/annurev.es.15.110184.001511

Raffel, M., Willert, C. E., Wereley, S., & Kompenhans, J. (2012). *Particle Image Velocity A Practical Guide*. *Journal of visualized experiments : JoVE*. https://doi.org/10.3791/4265

Raupach, M. R., & Shaw, R. H. (1982). Averaging procedures for flow within vegetation canopies. *Boundary-Layer Meteorology*, *22*(1), 79–90. https://doi.org/10.1007/BF00128057

van Rijn, L. C. (1987). Closure to " Sediment Transport, Part I: Bed Load Transport " by Leo C. van Rijn (October, 1984, Vol. 110, No. 10) . *Journal of Hydraulic Engineering*.

https://doi.org/10.1061/(asce)0733-9429(1987)113:9(1189)

van Rijn, L. C. (2007a). Unified view of sediment transport by currents and waves. I: Initiation of motion, bed roughness, and bed-load transport. *Journal of Hydraulic Engineering*. https://doi.org/10.1061/(ASCE)0733-9429(2007)133:6(649)

van Rijn, L. C. (2007b). Unified view of sediment transport by currents and waves. II: Suspended transport. *Journal of Hydraulic Engineering*. https://doi.org/10.1061/(ASCE)0733-9429(2007)133:6(668)

Roche, K. R., Blois, G., Best, J. L., Christensen, K. T., Aubeneau, A. F., & Packman, A. I. (2018). Turbulence Links Momentum and Solute Exchange in Coarse-Grained Streambeds. *Water Resources Research*, *54*(5), 3225–3242. https://doi.org/10.1029/2017WR021992

Santiago, J. G., Wereley, S. T., Meinhart, C. D., Beebe, D. J., & Adrian, R. J. (1998). A particle image velocimetry system for microfluidics. *Experiments in Fluids*. https://doi.org/10.1007/s003480050235

Schanderl, W., Jenssen, U., & Manhart, M. (2017). Near-Wall Stress Balance in Front of a Wall-Mounted Cylinder. *Flow, Turbulence and Combustion*, *99*(3–4), 665–684. https://doi.org/10.1007/s10494-017-9865-3

Shields, F. D., Bowie, A. J., & Cooper, C. M. (1995). Control of streambank erosion due to bed degradation with vegetation and structure. *JAWRA Journal of the American Water Resources Association*. https://doi.org/10.1111/j.1752-1688.1995.tb04035.x

Stapleton, K. R., & Huntley, D. A. (1995). Seabed stress determinations using the inertial dissipation method and the turbulent kinetic energy method. *Earth Surface Processes and Landforms*, *20*(9), 807–815. https://doi.org/10.1002/ESP.3290200906

Tanino, Y., & Nepf, H. (2008a). Lateral dispersion in random cylinder arrays at high Reynolds number. *Journal of Fluid Mechanics*, *600*, 339–371. https://doi.org/10.1017/S0022112008000505

Tanino, Y., & Nepf, H. M. (2008b). Laboratory Investigation of Mean Drag in a Random Array of Rigid, Emergent Cylinders. *Journal of Hydraulic Engineering*, *134*(1), 34–41. https://doi.org/10.1061/(ASCE)0733-9429(2008)134:1(34)

Tennekes, H., & Lumley, J. L. (1972, March 15). A First Course in Turbulence. The MIT Press. https://doi.org/10.7551/mitpress/3014.001.0001

Thielicke, W., & Stamhuis, E. J. (2014). PIVlab – Towards User-friendly, Affordable and Accurate Digital Particle Image Velocimetry in MATLAB. *Journal of Open Research Software*, *2*. https://doi.org/10.5334/jors.bl

Tinoco, R., & Coco, G. (2014). Observations of the effect of emergent vegetation on sediment resuspension under unidirectional currents and waves. *Earth Surface Dynamics*, *2*(1), 83–96. https://doi.org/10.5194/esurf-2-83-2014

Tinoco, R., & Coco, G. (2016). A laboratory study on sediment resuspension within arrays of rigid cylinders. *Advances in Water Resources*, *92*, 1–9. https://doi.org/10.1016/j.advwatres.2016.04.003

Tinoco, R., & Coco, G. (2018). Turbulence as the Main Driver of Resuspension in Oscillatory Flow Through Vegetation. *Journal of Geophysical Research: Earth Surface*, *123*(5), 891–904. https://doi.org/10.1002/2017JF004504

Trowbridge, J. H., & Lentz, S. J. (2018). The bottom boundary layer. *Annual Review of Marine Science*. https://doi.org/10.1146/annurev-marine-121916-063351

Türker, U., Yagci, O., & Kabdaşli, M. S. (2006). Analysis of coastal damage of a beach profile under the protection of emergent vegetation. *Ocean Engineering*, *33*(5–6), 810–828. https://doi.org/10.1016/j.oceaneng.2005.04.019

Vargas-Luna, A., Crosato, A., & Uijttewaal, W. S. J. (2015). Effects of vegetation on flow and sediment transport: Comparative analyses and validation of predicting models. *Earth Surface Processes and Landforms*, *40*(2), 157–176. https://doi.org/10.1002/esp.3633

Voermans, J. J., Ghisalberti, M., & Ivey, G. N. (2018). A Model for Mass Transport Across the Sediment-Water Interface. *Water Resources Research*, *54*(4), 2799–2812. https://doi.org/10.1002/2017WR022418

Ward, P. D., Montgomery, D. R., & Smith, R. (2000). Altered river morphology in south africa related to the permian-triassic extinction. *Science (New York, N.Y.)*, *289*(5485), 1740–1743. https://doi.org/10.1126/SCIENCE.289.5485.1740

Westerweel, J., & Scarano, F. (2005). Universal outlier detection for PIV data. *Experiments in Fluids*. https://doi.org/10.1007/s00348-005-0016-6

Wüest, A., & Lorke, A. (2003). Small-scale hydrodynamics in lakes. *Annual Review of Fluid Mechanics*, *35*(Section 3), 373–412. https://doi.org/10.1146/annurev.fluid.35.101101.161220

742 Xu, Y., & Nepf, H. (2020). Measured and Predicted Turbulent Kinetic Energy in Flow Through Emergent
743 Vegetation With Real Plant Morphology. *Water Resources Research*, *56*(12), 1–20.
744 https://doi.org/10.1029/2020WR027892

745 Yalin, M. S. (1977). Mechanics of sediment transport.

746 Yang, J., & Nepf, H. (2018). A Turbulence-Based Bed-Load Transport Model for Bare and Vegetated
747 Channels. *Geophysical Research Letters*, *45*(19), 10,428-10,436.
748 https://doi.org/10.1029/2018GL079319

749 Yang, J., & Nepf, H. (2019). Impact of Vegetation on Bed Load Transport Rate and Bedform
750 Characteristics. *Water Resources Research*, *55*(7), 6109–6124.
751 https://doi.org/10.1029/2018WR024404

752 Yang, J., Kerger, F., & Nepf, H. (2015). Estimation of the bed shear stress in vegetated and bare channels
753 with smooth beds. *Water Resources Research*, *51*(5), 3647–3663.
754 https://doi.org/10.1002/2014WR016042

755 Yang, J., Chung, H., & Nepf, H. (2016). The onset of sediment transport in vegetated channels predicted
756 by turbulent kinetic energy. *Geophysical Research Letters*, *43*(21).
757 https://doi.org/10.1002/2016GL071092

758